Title: Implantable Bioelectronics for Gut Electrophysiology

Authors: Alexander J. Boys[1,2]†, Amparo Güemes[3]†, Liang Ma[4], Rohit A. Gupta[5], Zixuan Lu[1], Chaeyeon Lee[3], Salim El-Hadwe[3,6], Alejandro Carnicer-Lombarte[3], Tobias E. Naegele[3], Friederike Uhlig[7,8], Damiano G. Barone[3,6], David C. Bulmer[5], Jennifer N. Gelinas[9,10,11] , Niall P. Hyland[7,8], Dion Khodagholy[4], George G. Malliaras[3]*, Róisín M. Owens[1]*

Affiliations:
[1]Department of Chemical Engineering & Biotechnology, University of Cambridge; Cambridge, UK
[2]Thayer School of Engineering, Dartmouth College, Hanover, NH, USA
[3]Department of Engineering, University of Cambridge, Cambridge, UK
[4]Department of Electrical Engineering, University of California, Irvine, CA, USA
[5]Department of Pharmacology, University of Cambridge, Cambridge, UK
[6]Department of Clinical Neurosciences, University of Cambridge, Cambridge, UK
[7]Department of Physiology, University College Cork, Cork, Ireland
[8]APC Microbiome Ireland, University College Cork, Cork, Ireland
[9]Department of Anatomy and Neurobiology, University of California, Irvine, CA, USA
[10]Department of Pediatrics, University of California, Irvine, CA, USA
[11]Children's Hospital of Orange County, Orange, CA, USA

†These authors contributed equally to this work.
*Co-corresponding authors: gm603@cam.ac.uk & rmo37@cam.ac.uk

Abstract:
The gastrointestinal tract is regulated by a complex network of electrically-active cell types that communicate to drive gut function. One of these systems, the enteric nervous system, represents a primary point of contact for a host of factors that influence bodily health and behavior. This division of the autonomic nervous system is unique in both its extensivity, with neurons distributed throughout the gastrointestinal tract from the esophagus to the rectum, and its capability for local information processing. However, the constant intrinsic and extrinsic motion of the gut as well as the sparse distribution of the neurons that constitute the enteric nervous system has made, access and analysis for study of this important component of the gastrointestinal tract exceedingly challenging. Here, we present the construction and validation of a bioelectronic implant for accessing neural information from the distal colon. The implant, constructed for compatibility with a novel surgical approach applicable across multiple species, is designed to be positioned within the colonic wall in close proximity to the enteric nervous plexi. We captured complex multi-frequency electrophysiological responses to neural chemical stimulants and showed that we can record distension activity mimicking gut motility. We also show the feasibility of utilizing this device for recording from putative single neurons in freely-moving rats and examining colonic activity in the context of food intake and stress. This work marks a significant advancement in understanding the complex pathways of the gut-brain axis. Our bioelectronic monitoring system demonstrates the power of real-time electrophysiological monitoring for the distal areas of the autonomic nervous system. Furthermore, direct access to the communication pathways of the enteric nervous system paves the way for novel neuromodulation strategies targeting the gut-brain axis.

Introduction

The gastrointestinal (GI) tract contains large networks of electrically-active cells that drive gut function through their interplay. Among these networks is the enteric nervous system (ENS), a network of sensory-, inter- and motor-neurons which plays a major role in controlling gut sensory transduction and motility, ion and mucus secretion, and vasodilation [1,2] . The ENS is also an essential part of the bidirectional gut-brain axis, affecting health and behavior [3,4], with many newly discovered connections to behavioral and pathologic changes elsewhere in the body [4–7]. Unlike other areas of the peripheral nervous system, the ENS is also capable of processing local information through reflex-like circuits that act independently of the central nervous system (CNS), for example, can coordinate simple peristaltic function independent of the central nervous system [1]. In addition to the ENS, the GI tract also contains electroactive pacemaker cells, called interstitial cells of Cajal (ICCs), that guide slow-wave gut motility, as well as a layered series of smooth muscle. The prominence of the gut-brain axis in human health, the relative independence of the ENS from the CNS and the possible role of the ENS as relay for gut-to-brain signaling, has made exploration of local gut electrophysiology timely.

The ENS is organized in two interconnected ganglionated plexi (myenteric and submucosal) that wrap circumferentially around the GI tract [1], with the former plexus situated between the outer muscle layers and the latter plexus in the submucosa. Given their positioning within the walls of the gut, these plexi are difficult to access in live animals. While genetically encoded calcium indicators, like GCaMP, enable non-invasive imaging of neuronal activity, their reliance on genetic modification limits their applicability in certain studies[8]. This issue, coupled to the limited and low-amplitude signaling from the electroactive cells in the gut adds further challenge to monitoring

the complex interplay of electrophysiological signaling within the gut. Traditional electrophysiological recording devices, like metal penetrating microelectrode arrays and silicon surface electrodes, are not compatible with the constant movements of the gut and fail to maintain conformal contact with the highly contoured and elastic tissue that constitutes the GI tract. As such, past studies have primarily focused on *ex vivo* recordings using organ baths, with patched electrophysiological setups, and / or calcium and voltage imaging [9–11]. Recent advances in the development of flexible bioelectronic probes have allowed for the construction of devices that are compatible with soft tissues and maintain a sustained electrical interface with local cell populations [12–14]. These devices function in an extracellular recording capacity, meaning that they can collect neural signals along with other electrophysiological inputs. Even with these advancements, few studies to-date, have been able to access intestinal tissue *in situ* using *in vivo* implantable technologies [15,16], with no current devices demonstrating successful *in vivo* recordings of ENS electrophysiology.

Here, we develop a custom and conformable bioelectronic implant system for conducting *in vivo* electrophysiological recordings within the colonic wall of rodents. First, we record local gut electrophysiology elicited in response to various *in vivo* mechanical and pharmacological stimuli in anaesthetized rodents. We then present an updated set of implants with integrated backend electronics and an associated surgical technique for performing recordings in freely-moving rats. This setup allowed us to examine the physiological electrical activity of the ENS and the colonic response to food intake and stress, discerning changes in electrophysiological response to both stimuli. We additionally show the scalability of these devices across multiple species, indicating their utility as a broad neuro-gastroenterological tool. This study opens up the potential to monitor ENS activity continuously in real time along the length of the GI tract, to not only increase our fundamental understanding of the ENS and GI physiology, but also to understand the gut-brain axis' influence on behavior.

Implant Design & Surgery Development

We designed an implantable bioelectronic device and associated surgery for recording electrophysiological signals from the gut *in vivo* (Fig. 1a,b). The devices are based on state-of-the-art bioelectronic photolithography microfabrication principles [13,17,18], utilizing a flexible, dielectric substrate for tissue contact (parylene-C) and a series of open recording gold electrodes coated with the conducting polymer, poly(ethylene dioxythiophene):poly(styrene sulfonate) (PEDOT:PSS), reducing impedance and therefore electrode size, for improved recording capabilities [19]. The devices were designed to meet the required size specifications to reside within the walls of the colon (see details in Methods) and a tetrode layout (Fig 1c) to resolve the neuronal clusters of the ganglionated plexi of the ENS [1]. We additionally included a series of markers and loops to assist in the surgical placement of the device in juxtaposition with the ENS.

For surgical access, we performed a laparotomy and isolated the colon from the surrounding tissue (Fig. 1d). To place the device, we ran a needle underneath the muscularis externa of the colon (Fig. 1e) and then back-tracked along this tunnel using a pair of reverse-action forceps (Fig. 1f). We then located and gripped the leading edge of the implant (Fig. 1g) and threaded the implant through the tunnel with the electrodes facing luminally to record from the submucosal plexus (Fig. 1h and i). The placement of the implant within the colonic wall also facilitates tight contact with tissue, even during acute and chronic recordings, as demonstrated below. The flexible device substrate

and the inherent elasticity of the gut tissue also limits the effect of blood, other accumulating fluids, and breathing interference on the quality of the electrophysiological recordings (Supplementary Movies 1 and 2). To confirm appropriate placement of the implant, we performed histology for device placement (Fig. 1e) into the colonic wall, identifying the positioning of the tunnel as luminally adjacent to the muscularis externa without perforating the gut wall or damaging the submucosal layers (Fig. 1j and Extended Data Fig. 1). To reduce interference from the myenteric plexus, we placed the insulating backing of the implant towards the muscularis externa, thereby also facing the electrodes towards the submucosal plexus of the ENS, which limits electromyographic signal contribution.

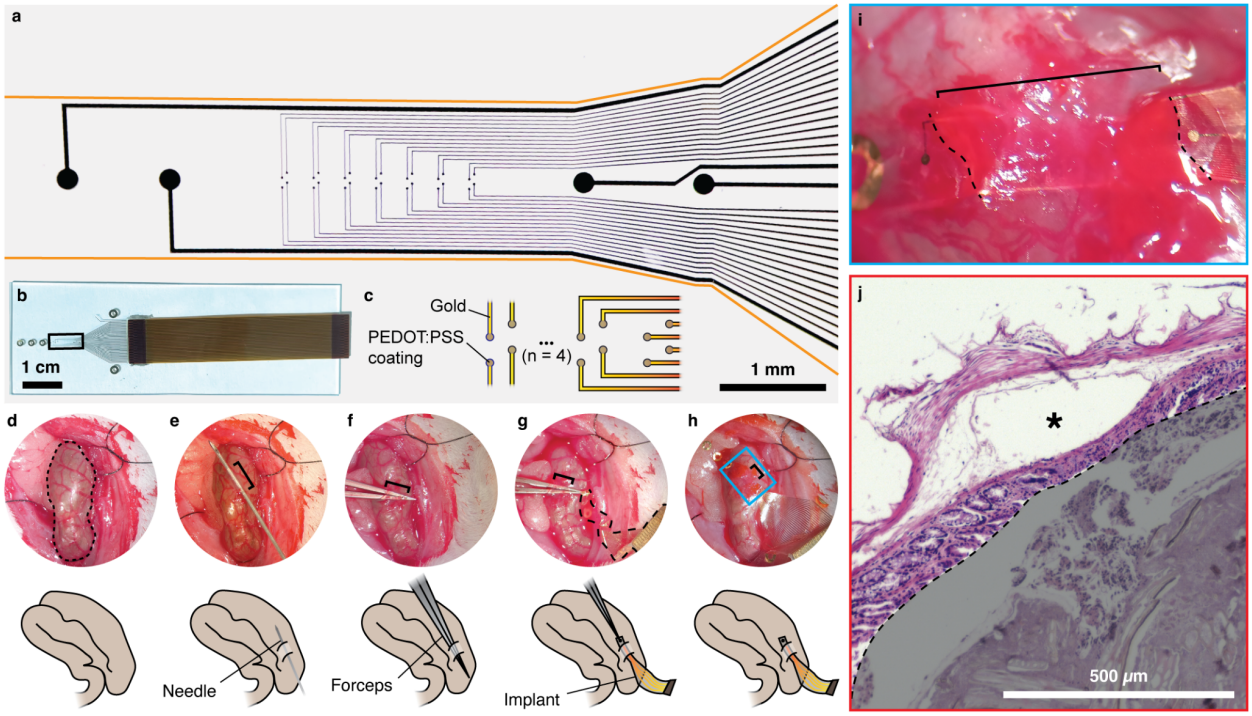

Fig. 1. Conformable devices can be surgically implanted on top of the submucosal plexus of the colon. a, Brightfield image taken in transmission showing the device layout for accessing the ENS. Devices consist of gold tracks insulated with parylene-C with PEDOT:PSS-coated gold electrodes, containing a central array of 28 recording electrodes, each 20 µm in diameter, flanked on either side by a pair of large electrodes, 200 µm in size, which are wired but were used as surgical markers. Given that the device substrate (parylene-C) is translucent, the outline of the device has been highlighted in orange. **b**, Photograph of device with bonded flat flexible cable (FFC) for connection to Intan recording system. Device is situated on a glass slide in this image for transport but is removed for implantation. Black box indicates region of device shown in **a**. Loops designed into the device for suturing are visible on the left, outside the red box. **c**, Schematic detailing recording electrode layout, where electrodes are arranged as a linear array of 7 tetrodes, with each electrode separated by 50 µm from its tetrode neighbors. **d-h**, Steps for implanting device into the colonic wall, images taken via stereoscope during surgery. Top shows surgical images of the steps, and bottom shows a representative schematic for each image. Dotted line in **d** indicates the periphery of the section of colon under analysis. Brackets in **e** indicate the section of needle that is situated in the wall of the colon. Brackets in **f**,**g** indicate the section of forceps that are within the wall. Dotted line in **g**, highlights the outer edges of the implant. Brackets in **h,i** show

the section of implant that is in the colonic wall. Inset from **h** in blue box is shown in **i** with device situated beneath the *muscularis externa*. Dotted lines indicate where the device enters (bottom dotted line) and exits (top dotted line) the tissue. **j**, Hematoxylin and eosin histological stain of needle placement in colonic wall, which is used to create the tunnel for the implant as shown in **e**. This image shows implantation directly below the muscularis externa. Asterisk indicates the tunnel in the tissue where the needle was threaded through the colonic wall. The lumen of the gut, which contains fecal matter is shaded in gray.

Distension of gut wall validates physiological responses to mechanical stimuli

During the passage of fecal matter through the colon, the gut wall experiences substantial strain, which activates stretch-sensitive neurons and drives a cascading peristaltic response [20]. To assess our device's performance, we initially analyzed the electrophysiological response of the colon to distension, validating the device's monitoring capabilities *in vivo* under anaesthesia. To initiate a distension, we ligated ~1 cm of colon to fluidically isolate this segment. We implanted the monitoring device as described above (Fig. 1d-i) and then, we placed a needle into the lumen of the colon in the vicinity of the implant (Fig. 2a) and injected ~0.3 mL of saline using a syringe pump, causing an increase in intraluminal pressure and distending the tissue (Fig. 2b and Supplementary Movie 3), while recording the evoked electrophysiological activity.

We performed two such distensions under low anaesthetic dose (1.3% isoflurane), increased the anaesthetic dose (5% isoflurane), and performed two further distensions. We examined the electrophysiological response at both high frequency (300-2000 Hz) and low frequency (0-300 Hz) (Fig. 2c) in 10 s windows after each distension. We observed an initial fast peak in the high-frequency trace (Fig. 2d), followed by an asynchronous extended voltage response, visible in the low-frequency trace (Fig. 2e) before returning to baseline. At the higher isoflurane dose (5%) neither high nor low frequency responses were observed (Fig. 2f and Extended Data Fig. 2a-f). This 'silencing' response may be explained by a direct reduction of neural activity[21,22] or by an anesthetic-induced muscle relaxation[23], leading to an elevated threshold for eliciting a response. In other words, the muscle's state of relaxation under the influence of higher doses of isoflurane may require a higher stimulus or pressure to activate neural responses. To examine the specific effects of the isoflurane anaesthetic, we also performed recordings using urethane, which is known to have limited neural suppression[24]. We observed a more consistent response (Extended Data Fig. 2g, h), but we found that the typical route of application for urethane through an intraperitoneal injection was infeasible for repeat experiments, given the location of the colon within the peritoneal cavity. The asynchronicity of the response also implies the action of multiple cell types in the construction of the resultant signal from mechanical distension. We hypothesize that the ICCs, crucial intermediates in the GI tract for bridging neurons to muscle tissue, may have significantly contributed to the recorded activity following distension. These specialized cells are not only integral to the coordination of peristaltic movements but also exhibit electrophysiological activity [25]. These experiments confirmed that recorded signals using this device setup are electrophysiological in origin and that these devices are capable of accurate recording in the dynamic colonic environment.

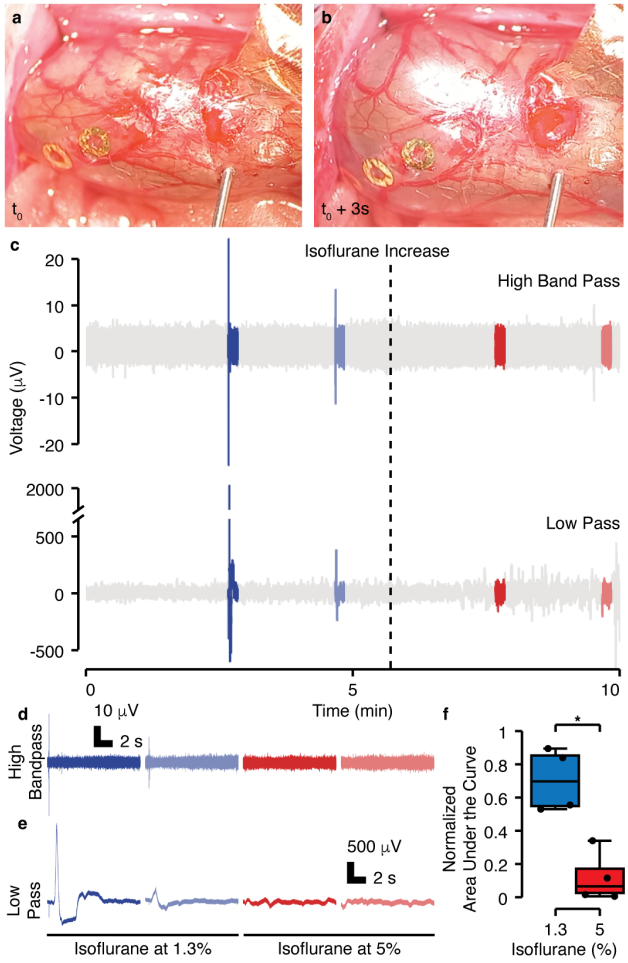

Fig. 2. Conformable electronics enable *in vivo* acquisition of gut electrophysiological responses to *in vivo* mechanical stimuli. a, Ligated portion of the colon with device implanted into the colonic wall prior to distension at t_0. **b**, Distended colon during saline injection. **c**, High-frequency bandpass (300 - 2000 Hz) and low pass (<300 Hz) representative full voltage traces. Segments highlighted in color represent the distension and following 10 s intervals after distension. Isoflurane was initially at 1.3% (blue) and was increased to 5% (red) at the time represented by the dashed line. **d**, Zoom in on the high-frequency bandpass traces corresponding to the distension segments. **e**, Zoom in on the low pass traces corresponding to the distension segments. **f**, Normalized Area Under the Curve (nAUC) for all the low-frequency distension traces (10 s window) before and after the rise in isoflurane concentration (n = 4 rats, see Extended Data Fig. 2a-f for traces from other rats). The nAUC standardizes the AUC obtained from each 10 s window by the range value within each experiment, ensuring a fair assessment of the responses across different rats. *: Statistically significant difference with $p<0.04$ using t-test after criteria for normality and variance homogeneity assumptions were met. The quantification of the nAUC for the high-frequency segments was not deemed meaningful due to the short duration of the response (<20 ms).

Pharmacological stimuli initiate multi-frequency electrophysiological response with common neurophysiological characteristics

Following successful recordings of distension-associated electrophysiological responses, we conducted further validation of the recording capabilities of our devices by capturing elicited compound activity in response to sensory neural stimulants under anesthesia (Fig. 3 and Extended Data Fig. 3). We recorded electrophysiological responses to the prototypic noxious inflammatory stimuli; bradykinin, an established chemical nociceptive stimulant relevant to tissue injury and pain which activates G-protein-coupled receptors [26], and activation by capsaicin, the active ingredient in peppers which activates transient receptor potential vanilloid type 1 (TRPV1) channels expressed on nociceptive sensory neurons [27]. Concentrations of 1 μM bradykinin, delivered topically (Fig. 3a), and 500 nM capsaicin, delivered topically (Fig 3b) or intraluminally (Fig 3c) were motivated by *ex vivo* electrophysiological recordings from lumbar splanchnic nerve (LSN) bundles in the mouse colon, which revealed colonic afferent responses to these mediators (Extended Data Fig. 3e, f). Drug additions were performed in sequence, beginning with bradykinin doses and followed by capsaicin doses (Extended Data Fig. 3a-c), to account for the known desensitizing properties of capsaicin [28]. Each administration, unless specifically noted for an experimental test, e.g. desensitization, was followed by multiple washes with saline and a waiting period of at least 5 minutes to reduce cross-effects from different drugs. The intermediate washes also provide a non-pharmacological comparative signal showing no response (Extended Data Fig. 3d).

Using this setup, we were able to record distinctive responses by examining the frequency-based power spectra (Fig. 3). Topical administration of bradykinin (Fig. 3a) occurred at t_0, followed by a brief period of inactivity (~10 seconds), then a burst of signal with a signal maximum around 1500 Hz at t_1, with a following low frequency increase at t_2, and return to baseline after ~90 seconds. Topical capsaicin (Fig. 3b) showed a similar delay and response suggesting sensory activation. Intraluminal capsaicin (Fig. 3c) resulted in a stronger response. In this case, the delay period shows some high-frequency activity before a broad-frequency response, likely due to differences in drug absorption versus topical as well as the change in administration route, before returning to baseline after 60 seconds. The initial transient high-frequency response is possibly linked to afferent sensory activation in the myenteric plexus and / or muscularis externa [29], complemented with the activation of TRPV1 receptors on submucosal neuroendocrine cells when injected from the luminal side [30], which then triggers the transmission of electrical signals between electrically coupled muscle cells through gap junctions, resulting in sustained high-firing activity. Changes are evident in the individual power spectra at different data points (Extended Data Fig. 4).

The population results were quantified by normalized metrics extracted from the temporal power spectral density (Fig. 3d) and compared to saline additions (Extended Data Fig. 3d), used as control and always registering the minimum response. The addition of bradykinin and intraluminal capsaicin resulted in a consistent substantial response, while the response to topical capsaicin varied in magnitude across animals. In all cases, some variability was observed between animals and administrations. This variability is likely due to challenges in precisely positioning the device within the colon wall, which affects proximity to neurons and electrophysiologically-active cells. Furthermore, while numerous capsaicin sensitive cells exist in the colon [31], not all neurons are capsaicin-sensitive [32], contributing to the heterogeneous responses observed between animals.

To examine whether repeated bradykinin additions induced measurable desensitization[33], using the same setup we added bradykinin multiple times to the same tissue, with or without a saline wash between additions. To perform this experiment, we added bradykinin topically to the tissue six times in total with the following scheme: bradykinin (1st), bradykinin (2nd), wash, bradykinin (3rd), bradykinin (4th), wash, bradykinin (5th), wash, bradykinin (6th). To analyze these data, we compared the first and third additions with the second and fourth additions (Fig. 3e), finding that back-to-back additions of bradykinin results in a trending decrease in signal intensity for the second response. We also compared the first, third, fifth, and sixth additions (Fig. 3f), finding that the response decreases after each, with a significant decrease observed for the first addition compared to the fifth and to the sixth additions. These data indicate a general desensitization of the neural response to bradykinin, as would be expected [33].

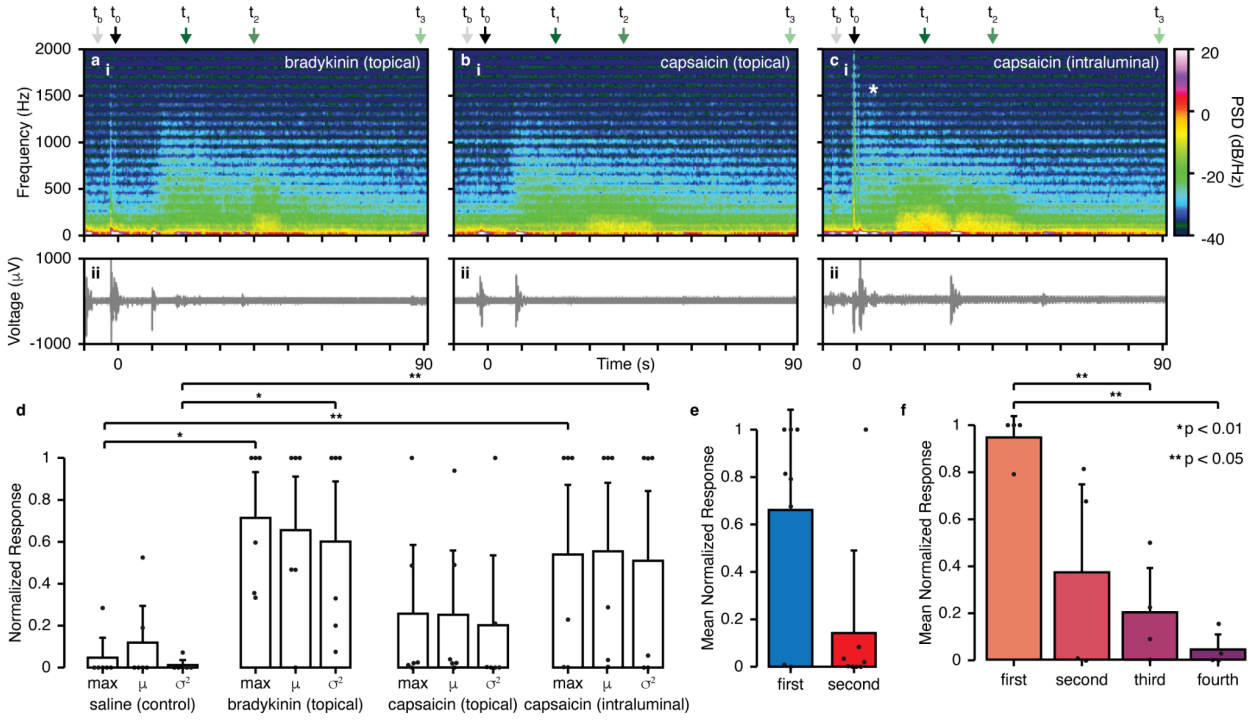

Fig. 3. Conformable electronics enable *in vivo* acquisition of distinct gut electrophysiological responses to various *in vivo* pharmacological stimuli. Representative responses for **a**, topical administration of 1 μM bradykinin, **b**, topical administration of 500 nM capsaicin, and **c**, intraluminal administration of 500 nM capsaicin (administered per the overall regimen shown in Extended Data Fig. 3), showing (**i**) spectrogram (0 - 2000 Hz) of power spectral density (PSD), (**ii**) raw voltage signal. Drug administration occurred at approximately t_0 for **a**, **b**, and **c**. Asterisk in **c** indicates initial high frequency response as discussed in the text. Power spectra corresponding to each data point t_b, t_0, t_1, t_2, t_3 in the spectrograms for each drug are shown in Extended Data Fig. 4. **d**, Normalized response per animal to different drug additions (n = 6 rats). The response activity elicited by each drug was quantified with the maximum [dB/(Hz*s)], mean [dB/(Hz*s)], and variance {[dB/(Hz*s)]^2} of the temporal power spectral density (PSD), computed as the area under the curve (AUC) of the spectrogram power data using non-overlapping 1 s rolling windows. The responses were normalized [0,1] to the maximum and minimum values obtained among all

additions (including saline) to allow for meaningful comparisons. **e**, **e**, **f,** Administration of bradykinin for **e** and **f** was performed as follows: 1st addition, 2nd addition, saline wash, 3rd addition, 4th addition, saline wash, 5th addition, saline wash, 6th addition. **e**, Mean of the temporal PSD (300 - 2000 Hz) for an initial and secondary administration of bradykinin (repeated twice, separated 2 to 3 minutes in between – 1st and 3rd additions compared to the 2nd and 4th) with no intermediate saline wash (n = 4 rats). **f**, Mean of the temporal PSD (300 - 2000 Hz) for 4 additions of bradykinin with at least one saline wash steps in between (n = 4 rats, – 1st addition compared to the 3rd, 5th, and 6th). Statistics for **d**, **e**, and **f** are detailed in the *Methods* and are shown in the figure as follows: * $p < 0.01$, ** $p < 0.05$. Isoflurane was kept at 1.3% for the whole duration of the recordings.

Extension of electrophysiological monitoring system to broader neuro-gastroenterological instances

Anaesthesia generally results in reduced spontaneous gut activity. However, during these and later procedures, we noted a few instances of visible spontaneous contractions that likely occurred in response to previous mechanical perturbation during surgery. We successfully recorded the electrophysiology response of one of these contractions (Extended Data Fig 5a, b) which was characterized as a large broad spectrum increase in electrophysiological power, which decreased back to baseline at the end of the visible contraction, approximately 1.5 min after initiation. The initial frequency maximum is approximately 1500 Hz, indicating a neuronally-driven response, followed by a lower maximum as well as increased signal intensity in sub-200 Hz frequencies (Extended Data Fig 5b). A clustering analysis of identified waveforms also shows particular waveforms which are only present in the signal during this contraction (Extended Data Fig 5a,d).

Finally, to showcase the broad usage and scalability of this device, we also demonstrated its utility in recording similar electrophysiological data in both mouse and pig colon under anesthesia (Extended Data Fig. 6). We show that we can perform similar tests in both larger and smaller species, achieving similar data types, indicating the extension of this platform as a scalable neuro-gastroenterological tool. Overall, the multifaceted nature of these signals underscores the complexity of neural interactions within the network. When evaluating the resultant signal in all cases, we observe distinct patterns of activation observed with different routes of drug administration, indicating the presence of various mechanisms of action, each exhibiting unique dynamics especially in the high-frequency components of the signals (neural activation). These observations, along with our results from mechanical distensions, confirm our capability for recording gut electrophysiology *in vivo*.

Chronic implantation of electrophysiological recording device enables high spatiotemporal probing of putative single neurons

Building on our successful validation of neural gut electrophysiology recordings in vivo under anesthesia, we shifted our focus to overcoming the limitations of anaesthetized recordings, particularly the strong suppression of spontaneous neural activity and the relative inactivity of the ENS under general anesthesia[34]. To truly understand the ENS within a fully functional gastrointestinal tract, we explored chronic recordings in freely moving animals. This approach allowed us to capture natural, spontaneous neural activity without the need for mechanical or chemical stimulation—an achievement not previously realized in unrestrained conditions.

To achieve chronic implantation of our devices, we modified the backend electronics, while maintaining the same tissue interface format we used for acute recordings (Fig. 4a, b). In this manner, electrode contact with tissue was preserved despite the substantial motion of the colon and surrounding tissues in a freely-moving rat. Data was extracted through a percutaneous shoulder connector that permitted tethering to an acquisition system during recording sessions. The recording ground electrode was situated within the subcutaneous tissue adjacent to the percutaneous port (Fig. 4c). We developed this approach in a pilot study (n = 2 rats), demonstrating feasibility for recording electrophysiological activity in freely-moving animals out to 2 weeks, (Extended Figure 7a-d). We also show the tissue response to the placement of this device (Extended Data Fig. 7e, f).

Using this experimental setup, we proceeded to monitor electrophysiologic activity across multiple 30 min recording sessions (n = 4 rats, 3 recording sessions up to 12 days after implantation) to analyze for specific neurophysiologic data and trends. Animal weight (Extended Data Fig. 8a) and implant impedance (Extended Data Fig. 8b-e) were monitored throughout the experimental period. Rats recovered remarkably well from surgery with no noted negative effects. Maintaining close anatomical proximity of the miniaturized, high efficiency recording electrodes to the submucosal plexus, through the use of the surgical technique from above (Fig. 1), opened the possibility of detecting neural spiking activity from the ENS. We also employed a tetrode-based electrode configuration (Fig. 1 and 4d), which is a geometric arrangement that facilitates differentiation of action potential waveforms from individual neurons. High pass filtering (>300 Hz) revealed bursts of high frequency activity that were restricted to nearby electrodes, suggestive of neural spiking (Fig. 4e). To investigate for putative activity patterns attributable to individual gut neurons, we adapted a thresholding and clustering approach commonly used with brain-derived electrophysiologic recordings [35,36]. We identified 89 putative single neurons across all recording sessions. These neurons displayed anatomically conceivable, localized spatial patterns of action potential waveforms across recording electrodes (Fig. 4f). Importantly, they also exhibited physiological spiking refractory periods (Fig. 4g), distinct patterns of co-activation with other neurons (Fig. 4h), and separable clusters of spatiotemporal action potential features in principal component space (Fig. 4i), supporting the characterization of this activity as representing individual neurons. Spikes from individual neurons were also detected across the time course of the session (Fig. 4j), indicating a stable interface between our device and the tissue.

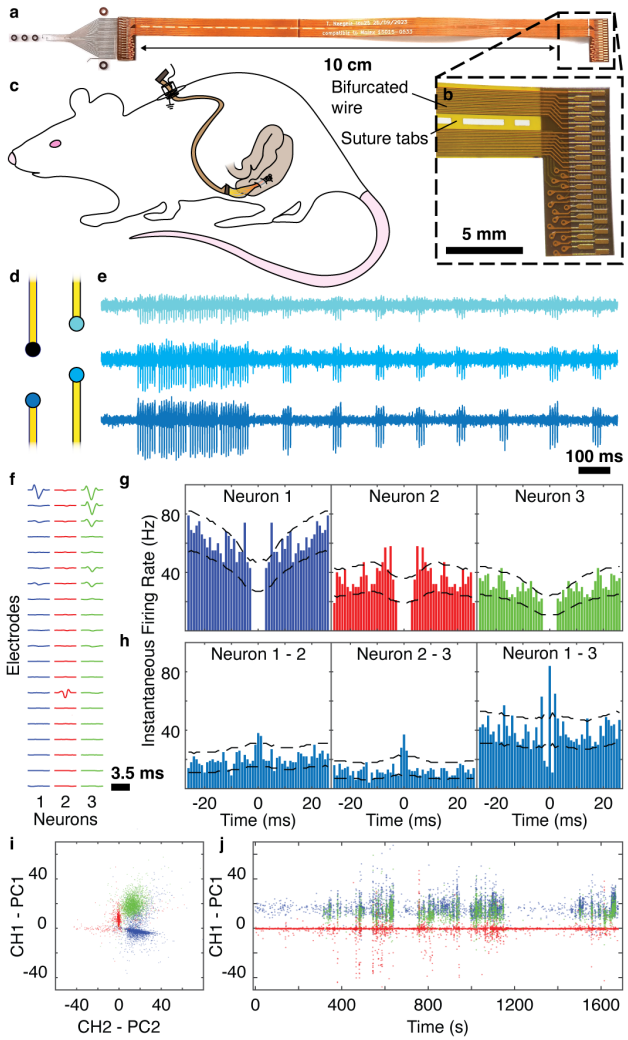

Figure 4. High spatiotemporal resolution electrophysiologic acquisition permits identification of putative single neurons in the enteric nervous system. a, Custom implantable wire was designed to facilitate chronic device implantation. The wire has two symmetric plugs / connectors, used to insert into a zero-insertion force (ZIF)-type plug (right), which via a custom-printed circuit board (PCB), can be interfaced with an Intan headstage for recording. The other end of the wire has an identical geometry but is bonded onto the microfabricated implant (left), which has the same replicated connector on the device itself. **b**, Inset showing plug with intermediate wiring visible on the left of the image. The intermediate wiring is double-sided to reduce footprint and bifurcated to allow for the placement of sutures around the wire. Small tabs connect the bifurcated wires across the length of the wire, enabling the wire to be anchored at the point where it crosses the peritoneal wall for access to the colon. **c**, Schematic detailing the placement of wiring and device within the rat. For the surgery, the wiring was routed subcutaneously between the percutaneous port down to the ventrolateral flank of the rat, where it crossed the peritoneal wall, allowing for implantation of the microfabricated portion of the device into the colon. **d**, Illustration of tetrode arrangement of four electrodes in one device in a chronically implanted rat. **e**, Sample high-pass filtered traces obtained during a recording session conducted 12 days post-surgery from three implanted electrodes (color refers to matching electrode in **e)** during (right; scale bar, 100 ms). **f**, Averaged extracellular spike waveforms for three sample putative single neurons recorded

at all implanted electrodes in the same chronic recording session demonstrating distinct and anatomically consistent localization across electrodes (n = 4718 spikes/neuron 1, 4748 spikes/neuron 2, 2497 spikes/neuron 3; trace, 3.5 ms). **g**, Autocorrelations of spike occurrence for putative single neurons shown in **b** demonstrate physiologic refractory periods. **h**, Cross-correlations of spike occurrence between putative single neurons reveal different co-activation patterns . **i**, Spatiotemporal features of putative single neuron activity form distinct clusters in principal component space. **j**, Spike occurrence attributable to putative single neurons is stable across a 30-minute recording session as visualized using example channel-projected principal components.

Conformable devices enable to record colonic responses to feeding and stress

The rats from the above electrophysiological analysis (n = 4) were used for behavioral recordings, where we recorded colonic electrophysiology in response to two key conditions: (1) acute stress induced by exposure to a novel environment for the first 15 minutes, followed by (2) the physiological response to food stimulus. At the 15-minute mark, Nutella® was introduced into the same environment (Supplementary Movie 4 and 5), allowing the rats to feed freely while recordings continued for at least another 15 minutes. Data were collected in the same manner on Days 1, 8, and 12.

We first analyzed the neural spiking patterns of putative individual gut neurons to feeding. We aligned the normalized instantaneous firing rate of each neuron to the onset of feeding and observed that most of the population exhibited an increase in activity within 2 minutes of this timepoint (Fig. 5a). Averaging the individual neuron responses to obtain a population measure revealed a significant enhancement of spiking in the post-meal compared to the pre-meal and meal epochs (Fig. 5b). A statistical comparison of putative single neuron average firing rate during pre-meal, meal, and post-meal epochs across 3 days of recording was found to be significant (Fig. 5c). These findings are in agreement with prior work indicating that enteric neural activity increases with food intake [37,38] and further support the ability of our device to capture physiologically relevant electrophysiologic signals from individual gut neurons.

Taking a broader, multi-cell approach, we investigated the gut response to a novel environment to assess anxiety-like behavior [39]. Given the expected widespread activation of diverse electrophysiological units present in the colon, including neurons, ICCs, and smooth muscle cells, we used a frequency band decomposition to capture and differentiate their distinct electrophysiological dynamics beyond isolated neural signals. We found that on Day 1 after implantation, the first time the animals were exposed to the novel environment (Fig. 5d), an initially large electrophysiological power is evident across frequency bands, especially within the first 5 minutes (Fig. 5e and Extended Data Fig. 9). This power trends downwards per minute as the rats spend further time in the environment. This electrophysiological behavior becomes less evident on Day 8 and Day 12 as the rats are exposed again to the same novel environment (Extended Data Fig. 9). This trend is notable when compiling the overall power for each frequency band across the first 15-minutes in the novel environment per day (Fig. 5f). We propose stress acclimatization [40] as a mechanism accounting for these observed data. Notably, different frequency bands temporally vary in an independent fashion, indicating the biologically-dense electrophysiological data collected from the colon with our devices (Fig 5e and Extended Data Fig. 10).

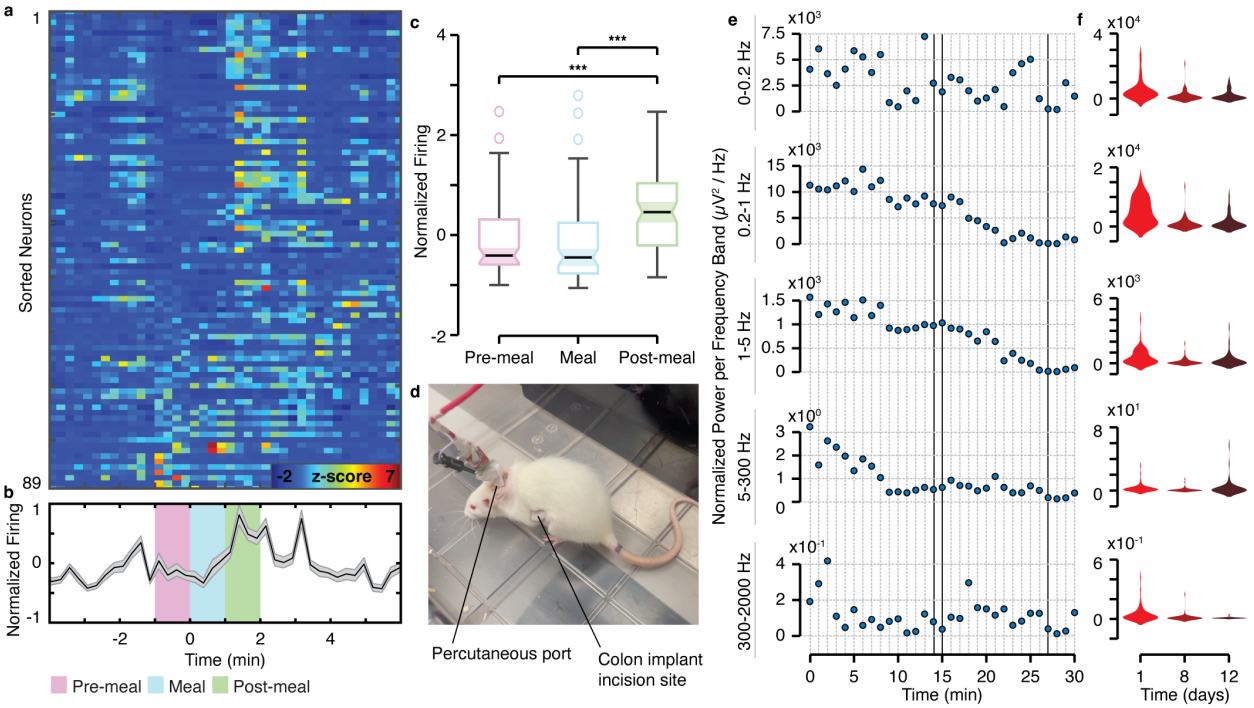

Figure 5. Colonic activity is modulated by food ingestion and stress. a, Normalized instantaneous firing rate of all putative single neurons aligned to onset of feeding and sorted by strength of pre-meal firing rate (warmer colors indicated higher z-scored firing rate modulation; n = 89 neurons, from 4 rats across 3 days of recording). **b**, Average normalized instantaneous firing rate of putative single neurons during pre-meal (magenta), meal (cyan), and post-meal (green) epochs (shaded error bars represent standard error of mean; n = 89 neurons, from 4 rats across 3 days of recording). **c**, Comparison of putative single neuron average normalized firing rate during pre-meal, meal, and post-meal epochs (Kruskal-Wallis ANOVA, $P = 4.25 \times 10^{-7}$; Wilcoxon signed-rank, pre-meal vs post-meal $P = 4.58 \times 10^{-6}$, meal vs post-meal $P = 1.90 \times 10^{-8}$; 89 neurons, from 4 rats across 3 days of recording; box center = medians; box edges = upper and lower quartiles; whiskers = non-outlier minimum and maximum; notch = 5% significance level). **d**, Image of rat in novel environment on Day 1. **e**, Traces showing the temporal evolution of the normalized power per frequency band (μV²/H) per minute for the full duration of the chronic recording for rat 1 on day 1. The frequency bands used were: "0 - 0.2 Hz" to capture slow wave activity associated with interstitial cells of Cajal (ICCs)[41]; "0.2 - 1 Hz" for slow rhythms such as those in circular smooth muscle[42,43]; "1 - 5 Hz" for faster rhythmic activities in smooth muscle[42,43]; "5 - 300 Hz" for primary skeletal muscle activity related to tissue and body movements (EMG related)[44]; and "300 - 2000 Hz" for high-frequency neural components[36,45–47]. **f**, Violin plots showing the distribution of the normalized power per frequency range (μV²/Hz) within first 15 minutes (data points) for all rats for each frequency band and day to visualize the decrease in the overall response along days.

Conclusion

In conclusion, we present a strategy and associated device for achieving neural recordings from the ENS in anaesthetized and freely-moving animals. Our data shows that rational design of bioelectronic devices coupled with surgical innovation allows access to traditionally difficult-to-

reach areas of physiology. The ENS presents a particularly challenging region of the nervous system to access, given its inherent susceptibility to suppression from anaesthetic agents, its location within a highly mobile and elastic tissue, and its disperse and somewhat sparse distribution (ganglionated plexi of nerves) within the walls of the GI tract. Utilizing current methodologies for flexible device fabrication, we were able to overcome these issues to record neural activity as well as other electrophysiological activity from the ENS. We further demonstrated the extended applicability of our device by successfully recording electrophysiological data from both mouse and pig colon highlighting its versatility across different species. We show the successful recording of putative single neurons in freely-moving animals as well as the overall electrophysiological response of cells residing in colonic tissue to nutritional intake as well as stress. These studies set the groundwork for exploring an important and consequential region of the nervous system and lay the framework for the democratization of neural recording technologies to the vast areas of the body that are supported by the peripheral nervous system.

Methods

Device Design

We designed our device to maximize likelihood of recording from the dispersed ganglia of the ENS. Unlike other areas of the nervous system, the ENS consists of a net-like configuration of interconnected ganglia. The inter-ganglionic spacing for proportions of the ENS in a rat is ~250 µm[48]. Given the inherent low-pass filtering properties of tissue[49], electrodes must be positioned in the vicinity of any high-frequency sources of interest in order to record these data. In the case of PEDOT:PSS-coated, gold microelectrodes, the effective recording volume for neural signals is within <50 µm radius[50]. As such, we positioned a series of 7 sets of 4 microelectrodes each in a linear fashion with an inter-set distance of 250 µm (Fig. 1a). This area combines for an effective measurement area of ~300 x 2000 µm, when considering the effective recording volume. We also included in the design a series of surgical markers, namely suture loops, to aid in chronic device placement, which are visible as gold rings, identifying the pass-through for a suture (Fig. 1b). In addition to these features, we also included a series of further design considerations based on potential utility for this device moving forward in future studies. For example, we wired in 4 large 200 µm diameter electrodes, which are suitable for applied electrical stimulation[51]. For this study, we used these as surgical markers to aid in implant positioning, but these electrodes are suitable for this application. We also arranged our microelectrodes into a tetrode configuration, which would theoretically enable the identification of single units [50]. However, we did not utilize this capability in this study, as successful single-unit analysis requires positioning the implant in very close proximity to a neuron (<50 µm). This proximity is particularly challenging in the enteric nervous system (ENS) due to its relatively low neuronal density, compared to the brain, where tetrode configurations are more commonly employed.

Implant Microfabrication & Integration

Implants were constructed as previously described [18] Parylene-C was deposited using a dimerized precursor, dichloro-p-cyclophane (Specialty Coating Systems, Indianapolis, IN, USA) onto a Si wafer at 2 µm thickness. Subsequently, wiring was patterned using AZ 5214 photoresist (Microchemicals GmbH, Ulm, Germany) and developed using AZ 351B (Microchemicals GmbH, Ulm, Germany). Gold deposition was performed at 100 nm with a electron beam Evaporator (PVD 75, Kurt J Lesker) using 10 nm of Ti as an adhesion layer to the parylene-C substrate. Gold tracks were patterned using a lift-off technique in acetone. A second parylene-C layer was deposited at 2

μm to insulate gold tracks. Following insulation, a second photolithographic step was performed to pattern the outline of the device using AZ 10XT photoresist (Microchemicals GmbH, Ulm, Germany) and AZ 400K developer (Microchemicals GmbH, Ulm, Germany). Using the photoresist as an etch-mask, the outline of the device was etched down to the Si wafer using a reactive ion etcher (RIE) (PlasmaPro RIE 80, Oxford Instruments, UK). A third layer of parylene-C was deposited on top of the device with an intermediate layer of soap, used as an anti-adhesive layer to facilitate coating of electrodes with PEDOT:PSS. After parylene-C deposition, a final lithographic step was performed to pattern the openings for the electrodes and connector array using AZ 10XT and AZ 400K developer, and the openings were etched using an RIE. Finally, a PEDOT:PSS mixture was spincoated onto the electrodes containing ethylene glycol (Sigma Aldrich, St. Louis, MO, USA), dodecyl benzene sulfonic acid (DBSA) (Sigma Aldrich, St. Louis, MO, USA), 3-glycidyloxypropyl trimethoxysilane (GOPS) (Sigma Aldrich, St. Louis, MO, USA), and PEDOT:PSS (Clevious PH 1000, Heraeus, Hanau, Germany). Patterning of the electrodes was accomplished using a peel-off technique. Finally, devices were removed from the Si wafer for bonding and integration with external electronic components. Implants were bonded (FINEPLACER pico2, Finetech GmbH, Germany) using an anisotropic conductive adhesive film (ACF) (10 μm particle size, 3T-TGP20500N, 3T Frontiers, Singapore) to flexible flat cables (FFCs) using either commercial FFCs (Molex, Lisle, IL, USA) or a custom FFC (Fig. 4a) that we designed and produced for chronic measurements.

Acute rat surgery & electrophysiological measurements

All experimental procedures were performed in accordance with the UK Animals (Scientific Procedures) Act 1986 and were approved by the animal welfare ethical review body at the University of Cambridge. These procedures were performed under a project license (PP5478947) by surgeons working with personal licenses, A.J. Boys (I00597808) and A. Güemes (I10076024), issued by the UK Home Office. Female Sprague-Dawley rats (purchased at 200 - 250 g) (Charles River Laboratories, Kent, UK) were primarily used, except in studies assessing the scalability of the devices in mice and pigs, as described below. The specifics of the surgical procedure varied with experiment, as is described above, but the following general protocol was used: Animals were anaesthetized for surgery using isoflurane inhalant. A small incision was made into the peritoneal cavity to access the colon, typically along the flank of the animal, and an implant was positioned within the wall of the colon. A secondary incision was performed to place a ground into the subcutaneous space above musculature on the contralateral side from the implant placement. The ground was positioned as distal as possible to avoid signal contamination from heart rate. The ground was consistent of a large area (~1 cm^2) PEDOT:PSS-coated gold pad with poly(imide) backing. We note that ground placement plays a substantial role in noise reduction for these recordings and should be carefully positioned to improve recording quality. With the grounding setup and the general implant placement, we also performed a thorough experimental assessment of potential sources of noise and interference to ensure that we did not misclassify mechanical artifacts as electrophysiological signal, specifically regarding the distension experiments but also as validation for the pharmacological experiments. These validations involved repositioning of the ground, tissue palpation, electrode repositioning, etc. Recordings were performed using an Intan Headstage (Intan Technologies, Los Angeles, CA, USA) and an Intan RHS Stim / Recording System (Intan Technologies, Los Angeles, CA, USA). These data were stored as Intan .rhs files, saved as 1-minute segments. The first step in processing the data in Python was to combine all these segments into a single file, which was then stored as a Parquet file for efficient access and

analysis. Injections were performed using a syringe pump (Legato®, KD Scientific, Holliston, MA, USA), and fluids were injected at a rate of 160 µL/s.

Mouse Study

All experimental procedures were performed in accordance with the UK Animals (Scientific Procedures) Act 1986 and were approved by the animal welfare ethical review body at the University of Cambridge. These procedures were performed under a project license (PP5478947) by surgeons working with personal licenses, A.J. Boys (I00597808) and T. Naegele (I68878875), issued by the UK Home Office. A female C57BL/6J mouse (Charles River Laboratories, Kent, UK) was used for this study. Implanted devices were of identical construction to those used for rats. To access the colon, a laparotomy was performed, and the device was inserted into the colonic wall as it was in the rat study portion of this work. A subcutaneous ground was placed in a secondary location as above. The colon was distended as it was in the rat study portion of this work. Recordings were performed using an Intan Headstage (Intan Technologies, Los Angeles, CA, USA) and an Intan RHS Stim / Recording System (Intan Technologies, Los Angeles, CA, USA). Data analysis was performed in the same manner as was performed for the rat mechanical stimulation portion of this work using a 4th order Butterworth in order to visualize the low frequency contributions of the smooth muscle response (0-300 Hz, lowpass filter with 300Hz cutoff frequency), and the high frequency activation contributions (300-2000 Hz, bandpass filter).

Pig Study

All experimental procedures were performed in accordance with the UK Animals (Scientific Procedures) Act 1986 and were approved by the animal welfare ethical review body at the University of Cambridge. These procedures were performed under project license (PP6076787) by surgeons working with personal licenses, S. El Hadwe (I54111393) and A. Carnicer Lombarte (IDA1CEDB9), issued by the UK Home Office. A female pig (50 kg) (Large White / Landrace cross) purchased from (B&S Farming Ltd. The Heath, Woolpit, Bury St Edmunds, Suffolk, IP30 9RN) was used. The animal was positioned in a supine position on the surgical table. A midline incision was made in the abdomen, beginning just below the sternum and extending toward the pelvic region. The abdominal wall layers were carefully dissected to access the abdominal cavity, and the abdominal organs were gently retracted to expose the large intestine. Identification of the ileocecal valve and cecum facilitated the localization of the large intestine. A segment of the colon was selected and isolated from the surrounding tissues using sterile techniques, preparing the region for implantation. For the implantation process, reverse micro-forceps were introduced through the abdominal wall, creating a tunnel for the neural interface device. Once externalized, the distal end of the tunnel allowed precise insertion and guided “pulling” of the implant through the passage. A metallic wire was secured to nearby muscle tissue to ensure proper grounding for neural recordings. Implanted devices were of identical construction to those used for rats. For capsaicin administration, 500 nM capsaicin was poured over the colon for ~1min while recording. Recordings were performed using an Intan Headstage (Intan Technologies, Los Angeles, CA, USA) and an Intan RHS Stim / Recording System (Intan Technologies, Los Angeles, CA, USA). For analyzing the impact on the tissue responses to capsaicin, the filtering process involved wide-bandpass filtering (0-2000 Hz) to visualize the complete frequency range of interest. The spectrogram of a window of 480 s after addition of the drug to the tissue was plotted to analyze the temporal and frequency responses of the tissue to capsaicin.

Ex vivo preparations & electrophysiology

Experiments using animal tissue were conducted on animals euthanized in accordance with Schedule 1 of the UK Animals (Scientific Procedures) Act 1986 Amendment Regulations 2012 under following approval from the University of Cambridge Animal Welfare Ethical Review Body. Adult male C57Bl/6 mice (10-12 weeks) were obtained from Charles River (Cambridge, UK; RRID:IMSR_JAX:000664). Mice were housed in temperature-controlled rooms (21°C) with a 12-hour light/dark cycle and provided with nesting material, enrichment (e.g., tubes, chewing blocks and shelters) and access to food and water *ad libitum*. Animals were euthanized by rising concentration of CO_2 or cervical dislocation, followed by exsanguination. Electrophysiological recordings of lumbar splanchnic nerve (LSN) activity were conducted as previously described[52,53]. Briefly, the distal colorectum (splenic flexure to rectum) and associated LSN (rostral to inferior mesenteric ganglia) were isolated from euthanized mice as described above. The colon was cannulated with fine thread (Gutermann) in a rectangular Sylgard-coated recording chamber (Dow Corning, UK) and bath superfused (7ml/min; 32-34°C) and luminally perfused (100µL/min) by a syringe pump (Harvard apparatus, MA) against a 2-3mmHg pressure with carbonated Krebs buffer solution (95% O_2, 5% CO_2) to keep the tissue alive. Krebs buffer was supplemented with 10µM atropine and 10µM nifedipine to prevent smooth muscle activity. Borosilicate suction electrodes were used to record the multi-unit activity of LSN bundles. Signals were acquired at 15 kHz at 20 kHz (Micro1401; Cambridge Electronic Design, UK) and exported to txt format with Spike2 (Cambridge Electronic Design, UK). Preparations underwent a minimum 30-minute stabilization period to ensure baseline firing was consistent.

Drug preparation and administration

Capsaicin (Tocris Bioscience, Bristol, UK) was dissolved in ethanol to yield a 1mM stock solution. The required volume of this stock solution was then diluted in 20ml of Krebs solution, resulting in a test solution with a concentration of 500nM. Bradykinin (Tocris Bioscience, Bristol, UK) was dissolved in distilled water to obtain a 10µM stock solution. The necessary volume of this stock solution was subsequently diluted in 20mL of Krebs solution, yielding a final test solution with an adjusted concentration of 1µM. Topical administration consisted of pouring drops at the location of the implant on top of the colonic tissue, whereas intraluminal doses consisted on delivering the solution into the adjacent luminal cavity using a syringe needle and a pump.

General analytical methodology

The raw signals undergo a sequence of filtering and characterization processes in the frequency domain, tailored to optimize the analysis for individual objectives and the collected data set. In general terms, each raw signal was first filtered using Butterworth filters of order 4 for high frequency or low frequency noise reduction (lowpass and bandpass filters respectively), with specific cutoff frequencies detailed in the relevant subsection for each experimental condition. Notch filters at 50 Hz and odd harmonics were applied when electrical contamination was significant, and specified in the respective section. For all the signals, the power spectral density (PSD) of the signals was computed using the Welch method with a segment length of 512 samples (non-overlapping). The Welch's method computes an estimate of the PSD by dividing the data into segments, computing a modified periodogram for each segment, and averaging these periodograms. This approach ensured a detailed analysis of frequency components while retaining the integrity of the original signals. Color map representations known as spectrograms were generated utilizing the Python function plt.specgram. These visualizations were meticulously set to 'psd' mode,

showcasing frequencies with a decibel ('dB') scale, ensuring an exact portrayal of frequency details. Spectrograms, unlike a simple Power Spectral Density (PSD) chart, offer a dynamic visual representation of how frequencies change over time in the signals. While PSD shows the strength of different frequencies at a single moment, spectrograms go further, illustrating how these frequencies evolve and interact across time. The methodology further involved the meticulous selection of specific windows of interest within the signal, enabling targeted and comprehensive investigation of crucial segments relative to each stimulation trial. The PSD and spectrograms for each of these segments were also computed, providing detailed frequency analyses to enhance the understanding of the data within these selected windows. The subsequent sections delve into the precise details of analysis and the criteria used to select parameters tailored to address each distinct experimental condition.

Analysis of drug stimulation trials

For analyzing the impact on the tissue responses to different chemical stimuli (i.e. drugs), the filtering process involved two strategies: wide-bandpass filtering (0-2000 Hz) to visualize the complete frequency range of interest, and tight-bandpass filtering (300-2000 Hz) with the addition of a notch filter to remove electrical noise to focus on the contribution of high frequency components in the signals. Using only the tight-bandpass filtered traces, windows of 10 s before and 90 s after addition of each drug to the tissues (locally or intraluminally) were extracted to analyze the temporal and frequency responses of the tissue to each drug. The analysis was divided into two strategies. To begin with, to evaluate temporal changes in signal frequency characteristics in each extracted window, a rolling AUC computation method was employed utilizing spectrogram data. The analysis involved iterating through columns of the power spectrum using a non-overlapping rolling window approach. The window size was calculated as the number of samples within the 1 s in the window. The AUC within each window of the spectrogram was carried out through numerical integration using the scipy.integrate.simps function from the SciPy library, and was plotted over time. Key metrics of the resulting temporal AUC such as the maximum, the mean and the variance of the AUC were computed and reported. These metrics offered insights into the dynamic changes and variability of signal characteristics within distinct temporal segments derived from the spectrogram analysis. For easy comparison across all injection experiments, each metric was normalized across the various drug types, guaranteeing their values fell within the 0-1 range for each experiment. Barplots were employed to illustrate the response based on the metrics to the four distinct drugs (BK, serosal capsaicin, intraluminal capsaicin, and wash-control). Additionally, in the recording featuring multiple BK additions, both consecutive and separated by wash additions, barplots of the metrics were computed to evaluate desensitization. Secondly, the Power Spectral Density (PSD) was derived from the computed power spectrum data obtained from the spectrogram at distinct time points: before the drug was introduced, immediately after its administration, and at the conclusion of the response. This approach was employed to offer a more comprehensive visualization, allowing for a clearer understanding of how frequency components evolved over time in response to the drug.

Analysis of contraction traces

A time window spanning 30 s before and 160 s after the visual initiation of the contraction was isolated across all channels. Similarly to the previous section, a wide and a tight bandpass traces were extracted and notch filter was applied. The spectrogram of the wide-bandpass filtering (0-2000 Hz) was plotted. From the tight-bandpass filtered traces (300-2000Hz), the envelope of these

signals was calculated to visualize the signal amplitude's progression during the contraction more clearly. This involved utilizing NumPy's Hilbert transform method to generate an analytic signal, from which the absolute value was derived to establish the signal's amplitude envelope. To enhance this envelope and minimize noise, a smoothing procedure was implemented using a 1 s rolling average window via convolution.

Analysis of distension stimulation

The distension dataset underwent two 4th order Butterworth filters: 1) low-pass filter with cut-off frequency at 300 Hz, chosen based on empirical evidence of activation of smooth muscle in the gut to be lower than 200-300 Hz[54], and 2) tight-bandpass filtering (300-2000 Hz). Notch filter was not needed as electrical noise was negligible. For the low-frequency bandpass signals, windows segment of 10 s after each distension was extracted for further analysis. The Area Under the Curve (AUC) was calculated for the positive part of all the extracted windows (low-pass filtered voltage traces) utilizing the trapezoidal rule (*trapz* method from the numpy library) for numerical integration. To enable consistent comparison across experiments concerning the four distention responses and particularly the variations pre- and post-increase in isoflurane, the normalized AUC (nAUC) was computed. This metric reflects the AUC for each distension segment, standardized by subtracting the minimum value and dividing by the range of the AUC observed across segments within each experiment (0-1). This normalization approach ensures a fair assessment of the responses across experiments. Statistical analyses were conducted using Python libraries scipy.stats, primarily employing two unpaired key tests: the t-test and the Mann-Whitney U test. These tests were applied for unpair comparisons between different groups or conditions within the dataset. The t-test was utilized to assess the significance of differences between means when the data met the assumptions of normality and homogeneity of variance, checked respectively using Shapiro-Wilk (for normality) and Levene's test (for homogeneity of variance). Conversely, the Mann-Whitney U test was employed for non-parametric analysis when the assumptions for the t-test were not met.

Chronic surgery & electrophysiology

Prior to surgery, rats were pre-conditioned to eat a commercial hazelnut-cocoa paste (Nutella) for 2 weeks. For chronic surgeries, female Sprague Dawley rats were anaesthetized using an isoflurane inhalant. Rats were given a pre-operative analgesic (Carprofen, Carprieve® Injection, Norbrook Laboratories) with a saline injection for fluid replacement. A primary incision to the subcutaneous musculature was made into the right flank of the rat approximately 1 cm distal to the rib cage. A secondary incision between the shoulder blades was made to the subcutaneous musculature. A tunnel was formed subcutaneously between these two incisions using blunt dissection, and the implant wiring was threaded through the tunnel, leaving the microfabricated portion of the implant on top of the musculature in the primary incision. Using a modified transcutaneous port (Vascular Access Button for rat, Linton Instrumentation, UK), stainless steel wire was threaded into the anchoring sponge of the port to form the ground for the subsequent recordings. The port was fitted into the secondary incision, the implant wiring was run through the port, and the pass through the port was back-filled with medical grade silicone (Kwik-Cast silicone, World Precision Instruments). The secondary incision was then sutured closed, and a Protective aluminum magnetic cap (Linton Instrumentation, UK) was placed over the port to prevent chewing on exposed wiring. At the primary incision, subsequent incisions were made through the subcutaneous musculature to access the peritoneal cavity. The colon was located in the vicinity of

the incision and the implant was placed into the wall of the colon, using the technique described above (Fig. 1d through h). The end of the implant was sutured into the wall of the colon using 9-0 non-resorbable sutures. The incision site was sutured in a layered fashion to bind the different layers of musculature around the implant wiring, using the interconnects that we designed into the implant wiring to anchor this peritoneal crossing in place. Finally, the primary was sutured closed, and the rats were allowed to recover. Rats were given post-operative analgesia each day (meloxicam, Metacam®, Boehringer Ingelheim Labs), through 3 days post-surgery. For the first subset of rats (n=2), recordings lasting over 1 hour were performed at Days 1, 7, and 14 to assess stability of the implants. At this point the rats were sacrificed, and the second rat's colon was examined and removed for histological preparation (Extended Data Fig. 8). The second subset of rats (n=4) was used for behavioral experiments. Rats underwent training prior to the surgery to consume a palatable food, Nutella® (3g). To standardize recording conditions, food was removed at 8 am on the day of recording, allowing for a minimum 4-hour period of food restriction. Each recording session over a period of up to 14 days was initiated by connecting the device to the acquisition system and moving the rat to a new environment (new cage) leading to stress response (Supplementary Movie 4). After 15 minutes, Nutella® was placed into environment recorded continued for at least 15 minutes after feeding. Recordings were conducted on Day 1, 8 and 12.

Single unit isolation & spatiotemporal analysis

Recordings were visually inspected for quality using Neuroscope. Epochs featuring synchronized high-amplitude sustained high-frequency activity consistent with EMG contamination[55], along with sharp voltage deflections indicative of mechanical/electrical noise, were manually identified and excluded from downstream MATLAB analyses. Recordings were high-pass filtered at 300 Hz. For each recording session, the 5 longest artifact-free epochs were used for each channel to calculate the noise floor, $noise\_floor = mean(\frac{|data|}{0.6745})$, [56]. A multiple of this noise floor (4-6, as curated by individual session data quality) was used as the threshold for detection of extracellular spikes. Negative peaks with amplitude greater than the threshold were detected as action potentials. Coincidental spikes across all channels were deemed as artifacts and removed from downstream analyses. Detected spikes were visually inspected alongside filtered raw recordings for veracity. Isolation of putative single neurons was done by inputting high-pass filtered recordings and detected spikes into KiloSort[57], and resulting clusters were visualized in Phy2. Clusters exhibiting physiologic refractory period, waveform characteristics and spatial profile were included in downstream analyses[58]. Auto-correlograms and cross-correlograms were obtained with temporal convolution of single-unit spike trains[59]. Repeated temporal shuffling of time bins were used to obtain 95% confidence intervals. Principal component weights calculated by KiloSort were used to demonstrate clustering in principal component space and stability over the course of a recording session[60].

Feeding electrophysiology analysis

Putative single neuron spiking was z-scored across each recording session to obtain normalized spiking rate patterns. Individual neuron spiking rates were calculated in 3 s bins, aligned to the onset of feeding, and visualized across the pre-meal, meal, and post-meal epochs. Use of bins ranging from 1 – 15 s did not alter conclusions. Population neural spiking activity was obtained by averaging the responses of all individual neurons in each epoch. Kruskal-Wallis ANOVA with post-hoc Wilcoxon signed-rank test and Bonferroni correction was used to determine statistical differences in population neural spiking between the epochs.

Stress-response multifrequency band analysis

The purpose of this multifrequency band analysis was to gain insights into the contributions of various biological sources to the recorded signals in the context of stress response. To start, we computed the average and standard deviation of the impedances for all working electrodes on each recording day and compared these metrics across different days. Channels that remained active across all recorded days were selected for further analysis. Signals from these selected channels were initially downsampled to 10 kHz to facilitate efficient processing. To minimize shared artifacts, signals were referenced to a common baseline; specifically, the mean signal across all selected channels was computed and subtracted from each channel's signal, producing a set of referenced signals. These referenced signals were then segmented into 1-minute intervals to analyze the temporal evolution of the signals. Within each interval, we divided the data into predefined frequency bands and applied bandpass filters to isolate these bands for detailed examination. The frequency bands used were: "0 - 0.2 Hz" to capture very low-frequency components and slow wave activity associated with interstitial cells of Cajal (ICCs); "0.2 - 1 Hz" for slow rhythms such as those in circular smooth muscle; "1 - 5 Hz" for faster rhythmic activities in smooth muscle; "5 - 300 Hz" for primary skeletal muscle activity related to body movements; and "300 - 2000 Hz" for high-frequency neural components. The frequency bands were chosen based on findings from electrogastrography (EGG)[42], research on interstitial cells of Cajal (ICCs) in ex vivo settings [41], and studies of electromyography[44,61] and extraneural activity [36,45–47]. Power Spectral Density (PSD) for each channel was computed using Welch's method, with a segment length of 1,000,000 samples to achieve a resolution of approximately 0.01 Hz, necessary for resolving the very slow frequencies of ICC cells. An overlap of 50% between segments was applied. The power within each frequency band was normalized by the bandwidth to allow for fair comparison across bands of different widths, labelled as normalized power per frequency range ($\mu V^2/Hz$) in the text. Visualizations were created to compare the evolution of power in each frequency band over time for each animal. Boxplots summarized the power profiles for all rats. Violin plots were also used to visualize the distribution of the normalized power per frequency range within first 15 minutes for all rats for each frequency band and day to visualize the response trend along days.

Acknowledgments: The authors would like to acknowledge Sam Hilton for supporting the animal work, and Sagnik Middya for his advice in backend electrical design and implementation. The authors would also like to acknowledge MRC Metabolic Diseases Unit (MC_UU_00014/5) for histological processing of paraffin-embedded sections. The views expressed are those of the author(s) and not necessarily those of the NIHR or the Department of Health and Social Care. For the purpose of open access, the authors have applied a Creative Commons Attribution (CC BY) license to any Author Accepted Manuscript version arising from this submission.

Funding:

HFSP Cross-disciplinary Fellowship [LT000034-C/2020] (AJB)
Royal Commission for the Exhibition of 1851 Research Fellowship, Royal Academy of Engineering Research Fellowship, Rosetrees Research Fellowship (AGG).
NIHR Cambridge Biomedical Research Centre [NIHR203312] (GGM)
US Airforce Office of Scientific Research (AFOSR) [FA8655-20-1-7021] (RMO)
Science Foundation Ireland [12/RC/2273_P2] (NPH, FHU)
Marie Skłodowska-Curie Action COFUND Programme (APEX) [754535] (FHU)

Cambridge Trust Fellowship (RAG)

Author contributions:
Conceptualization: AJB, AGG, RMO
Methodology: AJB, AGG, RAG, FHU
Investigation: AJB, AGG, RAG, ZL, CL, SE, AC, TN
Formal analysis: AJB, AGG, LM, JNG, DK
Visualization: AJB, AGG, LM
Code: AGG, LM
Funding acquisition: AJB, DCB, GGM, RMO
Project administration: RMO
Supervision: DGB, DCB, NPH, GGM, RMO
Writing – original draft: AJB, AGG
Writing – review & editing: AJB, AGG, LM, RAG, ZL, CL, SE, AC, TN, FHU, DGB, DCB, JNG, NPH, DK, GGM, RMO

Competing interests: The authors declare no competing interests.

Data and materials availability: All data, code, and materials used in this analysis are listed in the main text or the supplementary materials, are available on request, or have been uploaded to a repository.

References

1. Furness, J. B. The enteric nervous system and neurogastroenterology. *Nature Reviews Gastroenterology and Hepatology* vol. 9 286–294 Preprint at https://doi.org/10.1038/nrgastro.2012.32 (2012).
2. Spencer, N. J. & Hu, H. Enteric nervous system: sensory transduction, neural circuits and gastrointestinal motility. *Nat Rev Gastroenterol Hepatol* **17**, 338–351 (2020).
3. Borgmann, D. *et al.* Gut-brain communication by distinct sensory neurons differently controls feeding and glucose metabolism. *Cell Metab* **33**, 1466-1482.e7 (2021).
4. Cryan, J. F. *et al.* The Microbiota-Gut-Brain Axis. *Physiol Rev* **99**, 1877–2013 (2019).
5. Sampson, T. R. *et al.* Gut Microbiota Regulate Motor Deficits and Neuroinflammation in a Model of Parkinson's Disease. *Cell* **167**, 1469-1480.e12 (2016).
6. Morales-Soto, W., Gonzales, J., Jackson, W. F. & Gulbransen, B. D. Enteric glia promote visceral hypersensitivity during inflammation through intercellular signaling with gut nociceptors. *Sci Signal* **16**, (2023).
7. Zholos, A. V., Dryn, D. O. & Melnyk, M. I. General anaesthesia-related complications of gut motility with a focus on cholinergic mechanisms, TRP channels and visceral pain. *Front Physiol* **14**, (2023).
8. Rakhilin, N. *et al.* An intravital window to image the colon in real time. *Nature Communications 2019 10:1* **10**, 1–10 (2019).
9. Higham, J. P. *et al.* Transcriptomic profiling reveals a pronociceptive role for angiotensin II in inflammatory bowel disease. *Pain* **165**, 1592–1604 (2024).
10. Buckley, M. M. & O'Malley, D. Development of an ex Vivo Method for Multi-unit Recording of Microbiota-Colonic-Neural Signaling in Real Time. *Front Neurosci* **12**, (2018).

11. Vignali, S. *et al.* Recordings from human myenteric neurons using voltage-sensitive dyes. *J Neurosci Methods* **192**, 240–248 (2010).
12. Rochford, A. E. *et al.* Functional neurological restoration of amputated peripheral nerve using biohybrid regenerative bioelectronics. *Sci Adv* **9**, (2023).
13. Boys, A. J. *et al.* 3D Bioelectronics with a Remodellable Matrix for Long-Term Tissue Integration and Recording. *Advanced Materials* **35**, (2023).
14. Carnicer-Lombarte, A. *et al.* Ultraconformable cuff implants for long-term bidirectional interfacing of peripheral nerves at sub-nerve resolutions. *Nature Communications 2024 15:1* **15**, 1–14 (2024).
15. Efimov, A. I. *et al.* Remote optogenetic control of the enteric nervous system and brain-gut axis in freely-behaving mice enabled by a wireless, battery-free optoelectronic device. *Biosens Bioelectron* **258**, 116298 (2024).
16. Sahasrabudhe, A. *et al.* Multifunctional microelectronic fibers enable wireless modulation of gut and brain neural circuits. *Nat Biotechnol* (2023) doi:10.1038/s41587-023-01833-5.
17. Polyravas, A. G. *et al.* Effect of channel thickness on noise in organic electrochemical transistors. *Appl Phys Lett* **117**, (2020).
18. Oldroyd, P. *et al.* Fabrication of thin-film electrodes and organic electrochemical transistors for neural implants. *Nature Protocols 2025* 1–25 (2025) doi:10.1038/s41596-024-01116-6.
19. Khodagholy, D. *et al.* NeuroGrid: recording action potentials from the surface of the brain. *Nat Neurosci* **18**, 310–315 (2015).
20. Furness, J. B. & Costa, M. Types of nerves in the enteric nervous system. *Neuroscience* **5**, 1–20 (1980).
21. Silverman, H. A. *et al.* Standardization of methods to record Vagus nerve activity in mice. *Bioelectron Med* **4**, 3 (2018).
22. Nowicki, M. *et al.* Effects of isoflurane anesthesia on F-waves in the sciatic nerve of the adult rat. *Muscle Nerve* **50**, 257–261 (2014).
23. Kokita, N. *et al.* Potassium Channel-mediated Hyperpolarization of Mesenteric Vascular Smooth Muscle by Isoflurane . *Anesthesiology* **90**, 779–788 (1999).
24. Silverman, H. A. *et al.* Standardization of methods to record Vagus nerve activity in mice. *Bioelectron Med* **4**, 3 (2018).
25. Sanders, K. M., Koh, S. D. & Ward, S. M. Interstitial cells of cajal as pacemakers in the gastrointestinal tract. *Annu Rev Physiol* **68**, 307–343 (2006).
26. Liu, B. *et al.* The acute nociceptive signals induced by bradykinin in rat sensory neurons are mediated by inhibition of M-type K+ channels and activation of Ca2+-activated Cl– channels. *Journal of Clinical Investigation* **120**, 1240–1252 (2010).
27. Pasierski, M. & Szulczyk, B. Beneficial Effects of Capsaicin in Disorders of the Central Nervous System. *Molecules* **27**, 2484 (2022).
28. Szallasi, A., Cortright, D. N., Blum, C. A. & Eid, S. R. The vanilloid receptor TRPV1: 10 years from channel cloning to antagonist proof-of-concept. *Nat Rev Drug Discov* **6**, 357–372 (2007).
29. Zagorodnyuk, V. P. & Spencer, N. J. Localization of the Sensory Neurons and Mechanoreceptors Required for Stretch-Evoked Colonic Migrating Motor Complexes in Mouse Colon. *Front Physiol* **2**, (2011).
30. Matsumoto, K. *et al.* Distribution of transient receptor potential vanilloid 1 channel-expressing nerve fibers in mouse rectal and colonic enteric nervous system: relationship to peptidergic and nitrergic neurons. *Neuroscience* **172**, 518–534 (2011).

31. Virus, R. M. & Gebhart, G. F. Pharmacologic actions of capsaicin: Apparent involvement of substance P and serotonin. *Life Sci* **25**, 1273–1283 (1979).
32. Fitzgerald, M. Capsaicin and sensory neurones - a review. *Pain* **15**, 109–130 (1983).
33. Roberts, R. A. & Gullick, W. J. Bradykinin receptors undergo ligand-induced desensitization. *Biochemistry* **29**, 1975–1979 (1990).
34. Zholos, A. V., Dryn, D. O. & Melnyk, M. I. General anaesthesia-related complications of gut motility with a focus on cholinergic mechanisms, TRP channels and visceral pain. *Front Physiol* **14**, (2023).
35. Pachitariu, M., Sridhar, S. & Stringer, C. Solving the spike sorting problem with Kilosort. *bioRxiv* 2023.01.07.523036 (2023) doi:10.1101/2023.01.07.523036.
36. Khodagholy, D. *et al.* NeuroGrid: recording action potentials from the surface of the brain. *Nat Neurosci* **18**, 310–315 (2015).
37. Bayliss, W. M. & Starling, E. H. The movements and innervation of the small intestine. *J Physiol* **24**, 99–143 (1899).
38. Rogers, J., Raimundo, A. H. & Misiewicz, J. J. Cephalic phase of colonic pressure response to food. *Gut* **34**, 537–543 (1993).
39. Leigh, S. J. *et al.* The impact of acute and chronic stress on gastrointestinal physiology and function: a microbiota–gut–brain axis perspective. *J Physiol* **601**, 4491–4538 (2023).
40. Reed, M. D., Pira, A. S. & Febo, M. Behavioral Effects of Acclimatization To Restraint Protocol Used for Awake Animal Imaging. *J Neurosci Methods* **217**, 63–66 (2013).
41. Sarna, S. K. The gold standard for interpretation of slow wave frequency in *in vitro* and *in vivo* recordings by extracellular electrodes. *J Physiol* **591**, 4373–4374 (2013).
42. Chen, J.-D. Spectral analysis of electrogastrogram and its clinical significance. *http://www.wjgnet.com/* **2**, 9–11 (1996).
43. Ding, F., Guo, R., Cui, Z.-Y., Hu, H. & Zhao, G. Clinical application and research progress of extracellular slow wave recording in the gastrointestinal tract. *World J Gastrointest Surg* **14**, 544 (2022).
44. Desplenter, T. & Trejos, A. L. Evaluating Muscle Activation Models for Elbow Motion Estimation. *Sensors 2018, Vol. 18, Page 1004* **18**, 1004 (2018).
45. Güemes Gonzalez, A., Carnicer-Lombarte, A., Hilton, S. & Malliaras, G. A multivariate physiological model of vagus nerve signalling during metabolic challenges in anaesthetised rats for diabetes treatment. *J Neural Eng* **20**, 056033 (2023).
46. Marmerstein, J. T. Chronic recording of vagus nerve activity in rats using carbon nanotube yarn electrodes. (2022).
47. Jiman, A. A. A. Modulating and Monitoring Autonomic Nerves for Glycemic Control. *PhD Thesis* (2020).
48. Yip, J. L. K., Balasuriya, G. K., Spencer, S. J. & Hill-Yardin, E. L. Examining enteric nervous system function in rat and mouse: an interspecies comparison of colonic motility. *Am J Physiol Gastrointest Liver Physiol* **323**, G477–G487 (2022).
49. He, B. Neural Engineering: Third Edition. *Neural Engineering: Third Edition* 1–667 (2020) doi:10.1007/978-3-030-43395-6/COVER.
50. Hassan, A. R. *et al.* Translational Organic Neural Interface Devices at Single Neuron Resolution. *Advanced Science* **9**, 2202306 (2022).
51. Shannon, R. V. A model of safe levels for electrical stimulation. *IEEE Trans Biomed Eng* **39**, 424–426 (1992).

52. Peiris, M. *et al.* Peripheral KV7 channels regulate visceral sensory function in mouse and human colon. *Molecular Pain* **13** (2017).
53. Barker, K. H. *et al.* Sensitization of colonic nociceptors by TNFα is dependent on TNFR1 expression and p38 MAPK activity. *J Physiol* **600**, 3819–3836 (2022).
54. Crenner, F., Angel, F. & Ringwald, C. Ag/AgCl electrode assembly for thin smooth muscle electromyography. *Med Biol Eng Comput* **27**, 346–356 (1989).
55. Domínguez, S. *et al.* A transient postnatal quiescent period precedes emergence of mature cortical dynamics. *Elife* **10**, (2021).
56. Khodagholy, D. *et al.* NeuroGrid: Recording action potentials from the surface of the brain. *Nat Neurosci* **18**, 310–315 (2015).
57. Pachitariu, M., Sridhar, S. & Stringer, C. Solving the spike sorting problem with Kilosort. Preprint at https://doi.org/10.1101/2023.01.07.523036 (2023).
58. Li, Z., Boesmans, W., Kazwiny, Y., Hao, M. M. & Berghe, P. Vanden. Simultaneous whole-cell patch-clamp and calcium imaging on myenteric neurons. *Am J Physiol Gastrointest Liver Physiol* **323**, G341–G347 (2022).
59. Stark, E. & Abeles, M. Unbiased estimation of precise temporal correlations between spike trains. *J Neurosci Methods* **179**, (2009).
60. Ma, L. *et al.* High-Density, Conformable Conducting Polymer-Based Implantable Neural Probes for the Developing Brain. *Adv Healthc Mater* 2304164 (2024) doi:10.1002/ADHM.202304164.
61. Farina, D., Yoshida, K., Stieglitz, T. & Koch, K. P. Multichannel thin-film electrode for intramuscular electromyographic recordings. *J Appl Physiol* **104**, 821–827 (2008).